SAK

# REPORT DOCUMENTATION PAGE

Form Approved
OMB No. 0704-0188

Public reporting burden for this collection of information is estimated to average 1 hour per response, including the time for reviewing instructions, searching existing data sources, gathering and maintaining the data needed, and completing and reviewing the collection of information. Send comments regarding this burden estimate or any other aspect of this collection of information, including suggestions for reducing this burden, to Washington Headquarters Services, Directorate for information Operations and Reports, 1215 Jefferson Davis Highway, Suite 1204, Arlington, VA 22202-4302, and to the Office of Management and Budget, Paperwork Reduction Project (0704-0188), Washington, DC 20503

| 1. AGENCY USE ONLY (Leave blank) | 2. REPORT DATE | 3. REPORT TYPE AND DATES COVERED |
|---|---|---|
| | 96 May 29 | Final 93 Sep 25 - 96 Mar 24 |

**4. TITLE AND SUBTITLE**

A Study of Compressible Turbulence

**5. FUNDING NUMBERS**

F49620-93-C-0071

**6. AUTHOR(S)**

Robert E. Childs , Patrick H. Reisenthel

**7. PERFORMING ORGANIZATION NAME(S) AND ADDRESS(ES)**

Nielsen Enginering & Research, Inc.
526 Clyde Avenue
Mt. View, CA 94043-2212

**8. PERFORMING ORGANIZATION REPORT NUMBER**

2552/C

**9. SPONSORING/MONITORING AGENCY NAME(S) AND ADDRESS(ES)**

USAF, AFMC
Air Force Office of Scientific Research
110 Duncan Avenue, Suite B115
Bolling AFB, DC 20332-0001

NA

AFOSR-TR-96

0288

**11. SUPPLEMENTARY NOTES**

19960617 108

**12a. DISTRIBUTION/AVAILABILITY STATEMENT**

Approved for public release; distribution unlimited

**12b. DISTRIBUTION CODE**

**13. ABSTRACT** *(Maximum 200 words)*

Numerical simulations have been used to study the effects of compressibility on turbulence. Statistical and structural changes in turbulence are observed in both mixing layers and boundary layers due to dynamical compressibility effects. In mixing layers, the coherent large-scale vortices which dominate turbulent momentum transport change from being roughly spanwise at low convective Mach numbers to being oblique at elevated convective Mach numbers, roughly $M_c > 0.7$. Simulations of boundary layers have been performed up to M = 5, for adiabatic wall and mean-isothermal conditions; the latter is achieved by the computational artifice of deleting the mean dissipative heating. The mean-isothermal case experiences none of the classical compressible boundary layer effects, which are due to variable properties, and it increases the effective Mach number by lowering the near-wall sound speed. Numerous changes are observed in turbulent statistics and structures of the mean-isothermal flow, relative to low-speed flows. Perhaps the most striking change occurs in the structure of viscous sublayer streaks. The streaks are sinuous at low Mach numbers, but they become straighter at elevated Mach numbers. Features of the dilatation suggest that dynamical compressibility effects cause these changes.

| 14. SUBJECT TERMS | 15. NUMBER OF PAGES |
|---|---|
| Turbulence, Direct Numerical Simulation<br>Compressible Flow, Boundry Layer Flows | 33 |
| | 16. PRICE CODE |

| 17. SECURITY CLASSIFICATION OF REPORT | 18. SECURITY CLASSIFICATION OF THIS PAGE | 19. SECURITY CLASSIFICATION OF ABSTRACT | 20. LIMITATION OF ABSTRACT |
|---|---|---|---|
| UNCLASSIFIED | UNCLASSIFIED | UNCLASSIFIED | UL |



DTIC QUALITY INSPECTED 1

## 1. Introduction

The effects of compressibility in turbulent boundary layer flows are predominantly due to mean properties variation, up to $M_e = 5$ or more under adiabatic-wall conditions. In contrast, it is now widely, although not universally, accepted that the compressibility effects in high-speed mixing layers are due to dynamical compressibility processes which modify the structure of the large scale eddies. For example, aeroacousticians have long known of structural changes which occur in free jets above jet Mach numbers of $M_j \sim 1.4$ (Seiner 1984), which corresponds to convective Mach numbers near $M_c \sim 0.7$. This large difference in the principal causative mechanism of substantial changes in turbulence in high-speed flows is the cause of some interest. From a scientific viewpoint we know that a mechanism permitted by the governing equations can be significant in any flow, provided that the flow parameters are within certain ranges. Properties variation effects do occur in mixing layers, but the evidence for dynamical compressibility effects modifying turbulent structures has been tenuous (Spina et al 1994). Because of the magnitude of the structural and statistical changes in mixing layers, it is important to understand how related changes could occur in boundary layers.

The ability to meet the broad objectives of aerospace research and development requires a better understanding of compressibility effects on turbulence across all significant types of flow phenomena. This is especially true because turbulence is increasingly important to flight vehicles at elevated Mach numbers, and future flight vehicles are envisioned which will operate at higher speeds and/or for more prolonged durations at elevated speeds than current vehicles. These conditions place greater demands on the vehicle design. Thus, the thermal and mechanical properties of boundary layer transition and turbulence must be known with greater precision. From a very practical standpoint, turbulence modeling which works well for boundary and mixing layers and a variety of other types of flows is needed to make accurate predictions of realistic flight vehicles, but it does not yet exist.

### Objectives

The broad goal of this work is to gain an understanding of the physics of turbulence at very high Mach numbers, excluding chemical and rarefaction effects. The particular focus of the work is on dynamical compressibility effects which occur in high-speed mixing layers, rather than on the mean properties variations which dominate boundary layer behavior. A specific goal of the work is to determine if the theories for compressibility effects in mixing layers and boundary layers can be unified.

## 2. Simulation Methodology

The CFD methods used to simulate high-speed turbulence should possess high accuracy and the ability to capture shocks. High accuracy here means that, for a wide range of length scales, especially the convective terms but also the viscous terms must be accurately represented, and any "inappropriate" algorithmic dissipation must be negligibly small. For fundamental reasons, the ability to capture shocks tends to conflict with high accuracy, but both features must be achieved. As a practical matter, computational efficiency is also important. This section describes the numerical methods used in this work. The key features of the Navier-Stokes solver are highlighted here, and the noteworthy aspects are described below in more detail.

1. Finite-volume discretization is used on stretched Cartesian grids.

2. Central discretization of convective and viscous terms is done with a factored scheme, that is, the three-dimensionality is split into three one-dimensional interpolation and derivative operators.

3. All of the spatial operators are optimized to maximize their bandwidths, that is, the range of length scales (Fourier wave number) which are resolved to some reasonably tight error tolerance. The optimized spatial operators are not formally high order, but they are high accuracy, which is a feature common to apparently all schemes (Lele 1992, Tam 1993, Zingg 1993) optimized for efficiency.

4. While the optimized convective terms yielded significant gains in accuracy, the ones must critical to accuracy and computational efficiency were in the artificial dissipation.

5. Shock capturing was enabled with a nonlinear high-order/low-order artificial dissipation.

6. An explicit third-order Runge-Kutta scheme was used for temporal integration.

**Optimized Spatial Schemes** - Optimized spatial discretization is used for the interpolation, derivative, and dissipation operators used to compute the average cell-face flux. Optimization contributes significantly to the accuracy of the discretization and thus to efficiency of the numerical method. This section describes the optimized schemes and the improvements in accuracy that are obtained via optimization.

In the factored finite-volume scheme used here, cell-face fluxes are constructed from a linear weighted sum of the cell-averaged solution or flux values in adjacent cells. Those discretization weights determine the properties of the numerical scheme, and the weights can be determined by any of several methods. Typically a "high-order" method is one derived using Taylor series, and the weights are selected so that a solution described by a polynomial of some order is treated exactly by the high-order method. Equivalently, the order of the method is the leading order error term in a Taylor series expansion of the scheme. These methods have the property that the error decays as a certain power of the grid spacing, for small grid spacing: $\Delta x \rightarrow 0$. The

higher the order of the method, the greater its asymptotic convergence rate and perceived quality.

However, high-order is not the most important property for typical applied CFD work. For fluid dynamical problems with a broad energy spectrum, and especially in turbulence, global accuracy is more strongly affected by large differences in the accuracy at small scales of motion, than in very small differences in errors (e.g., $10^{-5}$ versus $10^{-8}$) incurred in low wave number modes. Thus, the optimized schemes used here are constructed to maximize the bandwidth which is processed to the desired accuracy, with less concern for the formal order of the method.

Various methods have employed the concept of optimization. Lele (1992) used optimization in conjunction with Pade approximants to derive a set of schemes with accuracy nearly up to that of full Fourier methods (not dealiased). Tam and co-workers (1993) applied the name "dispersion-relation-preserving schemes" to their optimized schemes because the methods were used in acoustics calculations, and the optimized schemes reduce dispersion over their well-resolved bandwidth.

The normalized discretization error of several Taylor Series and optimized high accuracy schemes are given in Fig. 2.1 for the finite-volume approximation of convection, which is constructed from the difference of fluxes interpolated to the cell faces. The normalization is such that an error magnitude of unity represents zero accuracy: the discrete first derivative is zero despite its actual value. Wave numbers are normalized so that $\omega=\pi$ corresponds to the highest frequency representable on a grid. The errors in the discretization scheme are computed using conventional Fourier analysis methods; the phase angle which generated the greatest error magnitude was used to provide data for these figures.

The highest bandwidth (range of well-resolved wave numbers) on this plot is achieved with the optimized 10-point interpolation used to compute the cell-face flux. Its error is less than $10^{-3}$ up to $\omega=0.55\pi$, which is a 33% increase in bandwidth over the Taylor series scheme with the same number of points in the stencil. The criteria used to develop the optimized schemes in these figures sought to maximize the bandwidth defined by the minimum wave number at which the error first exceeded $10^{-3}$, while tolerating very small errors (e.g., $<10^{-5}$) at low wave numbers. That this objective was achieved can be seen in Fig. 2.1. Asymptotically, these particular optimized schemes are second-order accurate, but that too is the user choice. One feature to note in the optimized schemes is that the error goes to zero at a few wave numbers. The optimized schemes are combinations of several polynomial schemes, and they have roots at a few different wave numbers. The Taylor series schemes also have several roots, but they are all at $\omega=0$.

Optimized discretization was also developed for the viscous terms. The accuracy of viscous terms was generally equal to or greater than the accuracy of the convective terms.

Optimized and conventional central artificial dissipation schemes are given in Fig. 2.2. The characteristics of the dissipation versus wave number are generally similar to error characteristics for the convective terms. The most notable feature, and the one which motivated the development of the optimized dissipation can be seen in this figure. The eighth-order Taylor-

series dissipation reaches $10^{-3}$ at $\omega=0.25\pi$. The level at which dissipation becomes significant is not known and is certainly problem-dependent; $10^{-3}$ is an arbitrary but not unreasonable dividing line between significant and insignificant level of dissipation. A value of $\omega=0.25\pi$ is too low of a number wave to willingly suffer appreciable dissipation in a turbulence simulation. In contrast, the optimized 10-point dissipation reaches $10^{-3}$ at $\omega = 0.51\pi$. This doubles the relatively undissipated wave number range compared to eighth-order dissipation in one dimension; in a three-dimensional turbulence simulation, it increases by a factor of $2^3$ the number of modes resolved free of significant dissipation. Switching from the standard eighth-order to the optimized ten-point dissipation was responsible for a significant improvement in the quality of the simulations. Another feature of the optimized dissipation is that negative dissipation (amplification) is unacceptable. Thus, while the sign of the error in convective terms is relatively unimportant, the sign of the dissipation is critical. Where appropriate, each real root of the polynomial in the dissipation was placed very close to one other root; this approach gave a good bandwidth and vanishingly small levels of negative dissipation. As with the optimized convective terms, different optimization criteria might be more relevant for CFD problems other than turbulence simulations.

The bandwidth of dissipation operators should be of particular concern in schemes which use low-order unoptimized dissipation. For example, the fourth-order dissipation commonly used in steady-state calculations has relatively poor bandwidth of roughly $0.1\pi$. Also, the so-called ENO (essentially nonoscillatory) schemes rely on biased discretization stencils, which implicitly contain intermediate-order (e.g., 4th- to 6th-order) dissipation which will reach the $10^{-3}$ threshold well below $\omega=0.25\pi$.

High-accuracy boundary conditions and near-boundary discretization are also required to maintain the accuracy of the interior scheme. In the present simulation, periodic conditions were used in both directions parallel to the wall. The periodic boundaries were treated with the same discretization schemes as the interior. Viscous wall boundary conditions and nonreflecting far-field conditions are the other boundary conditions. Normal to the wall, the accuracy applied to the discretization of physics terms "runs out" to low (second) order. This has the disadvantage of failing to preserve the bandwidth of the interior scheme. However, the physics of near-wall turbulence is generally compatible with this treatment. The near-wall mean velocity is linear, and the fluctuating velocities are linear or quadratic (e.g., $u^+\sim y^+$, $v^+\sim y^{+2}$), and the grid is clustered significantly normal to the wall. The second-order boundary conditions are also compatible with this near-wall physics. Thus, good simulation accuracy can be preserved without a high-bandwidth down to and normal to the wall. A first-order implementation of Thompson's nonreflecting boundary conditions was used at the far-field boundary, and it appeared to perform adequately.

The artificial dissipation is potentially a greater problem at nonperiodic boundaries, since there are no compact approximations of high-order dissipation. (E.g., there is no three-point eighth-order dissipation formula.) Using low-order dissipation near to and normal to the wall is unacceptable because of its poor wave number properties. That form of dissipation would carry much of the true viscous stresses and severely damage the accuracy of all viscous processes. In

the present study, the simplest solution was to "turn off" the artificial dissipation near to and normal to the wall. The optimized 10-point dissipation was still used in both directions parallel to the wall.

**Factoring Errors** - The potential errors incurred by factoring the multi-dimensional finite-volume equations into multiple one-dimensional operations are also a concern. A limited analysis of this issue has been performed in two-dimensions (Childs, 1993), and limited to cartesian grids. For one-dimensional interpolation in the x-direction, nonuniformity in the y-direction canceled exactly for the integrated cell-face flux, up to quadratic variations in y, the highest order examined. Computational tests confirmed that the finite-volume multi-dimensional bandwidth is as good as the bandwidth of the one-dimensional operators. Numerous analytical studies have examined the errors associated with factored finite-difference schemes and found them to be anisotropic, but with the greatest errors occurring *along* each grid axis, rather than as along some non-grid-oriented angle. Therefore, factoring errors on cartesian grids are suitably small. On typical curvilinear structured grids, in which metrics transform the grid and governing equations, the cartesian-grid error properties are recovered, less the bandwidth of the grid metrics (Childs 1993). Thus, a smooth grid is required to retain high accuracy on curvilinear grids, but then the multi-dimensional accuracy also remains good.

**Other Nonlinearities** The nonlinearity in the Navier-Stokes equations due to the variable fluid properties, density, viscosity, and in the state equation, may become increasingly important at elevated Mach numbers. The effects of properties variations have been examined by Huang (1995) and found to be small up to M = 3 in an adiabatic-wall turbulence flow. We comment here on one algorithmic issue which has not been widely discussed.

In finite-volume numerical schemes, the solution is represented by cell-integrated values of the solution. The conservative variables are [$\rho$, $\rho u$, $\rho v$, $\rho w$, $\rho E$]. Several terms required to compute the fluxes of the conserved variables, including the pressure and even the velocities, are nonlinear functions of the conservative variables. Where the conservative variables vary nonlinearly across a cell, then the cell-averaged velocity or pressure, $\overline{u}$ or $\overline{p}$, are not computed accurately using standard formulae, that is, $\overline{u} \neq \overline{\rho u}/\overline{\rho}$, in general. (These issues also provided the motivation for Favre-averaging.) All of the numerical fluxes needed to numerically integrate the governing equations, except for the mass fluxes, are nonlinear functions of the conservative variables. A one-dimensional analysis of the expression for $\overline{u}$ was performed in which the variation of the solution across a finite volume cell was accurately accounted for, and the error was found to be $O(\Delta x^6)\,\rho'' \rho u'' / \rho\, \rho u$ , in which $()'$ denotes differentiation with respect to x. Thus, the error depends on the magnitude of the variation of the solution about its mean, and on the grid spacing. The scaling on $\Delta x^6$ means that the error is of "high order," but this term does not lead directly to the degradation of the algorithm's bandwidth. The accuracy of the scheme will also be strongly affected by terms like $\rho''/\rho$. Apparently, the relative error in computing small values of $\overline{u}$ could be very large. In the present work, equations like $\overline{u} = \overline{\rho u}/\overline{\rho}$ are used without corrections, but we note that further improvements may be appropriate.

**Mean-Isothermal Boundary Layer** - It well known that many of the compressibility effects in boundary layers are due to mean aerodynamics heating. These effects are strong and can obscure the weaker effects due to dynamical compressibility. With simulations, it is possible to remove the effects of mean heating while leaving the dynamics of the flow otherwise unaffected. A mean isothermal boundary layer is one in which the thermal energy of dissipative heating is removed, so that the flow has a (very nearly) uniform mean static temperature. This step should permit a more "unobstructed view" of dynamical compressibility effects in boundary layers.

The widely accepted Van Driest theory for high-speed boundary layers predicts that a mean-isothermal boundary layer will be unchanged from its equivalent incompressible flow.

Another consideration is that higher effective Mach numbers are achieved with mean heat removal. In an adiabatic-wall boundary layer the near-wall temperature is very roughly equal to the stagnation temperature. The sonic speed in this fluid can be substantially higher than that in the freestream so that the effective Mach number, the freestream velocity divided by some appropriate sound speed in the boundary layer, is less than the freestream Mach number. The effective Mach number obtained by using the stagnation temperature to compute the sonic speed never exceeds M = 2.3 in adiabatic flows.

Mechanics of Heat Removal - The goal in removing heat from the boundary layer is to cause no direct modification of the fluctuating quantities, while removing only the mean dissipative heating. This goal is achieved by adding a thermal "sink" term to the energy equation of the form:

$$S(y) = -c_s\,(\langle T\rangle - T_e) \qquad (2.1)$$

in which <T> represents the average temperature in planes parallel to the wall, $T_e$ is the target temperature, and $c_s$ is an empirically selected rate coefficient which is large enough to drive <T> almost to $T_e$, but not so large as to cause instability of the temporal integration scheme. The thermal energy removal is uniform in planes, based on the planar average temperature, and temperature fluctuations were not directly affected by this energy sink.

**Calculation of Statistics** - Turbulent statistics are computed over a short-interval time series of "snapshots" of the turbulent flow, in addition to the spatial integration over the mean-invariant planes parallel to the wall. Inner-wall scaling was used to normalize virtually all statistical results, and the small evolution in the inner-wall scaling was accounted for when integrating statistics with respect to time. Typical temporal integration extended over ten or more realizations of the instantaneous solution, over a time interval corresponding to a particle in the freestream convecting roughly five boundary layer thicknesses. Averaged quantities are denoted by the usual "overbar" in the text, but by brackets, <>, in the figures, due to the capabilities of the plotting software used for this work.

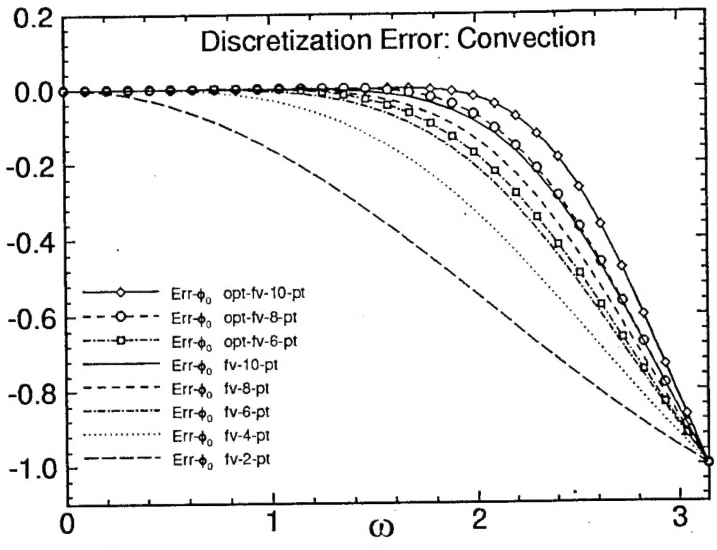


Figure 2.1(a) Error versus wave number for several finite-volume Taylor series and optimized approximations of a first derivative (linear coordinates).

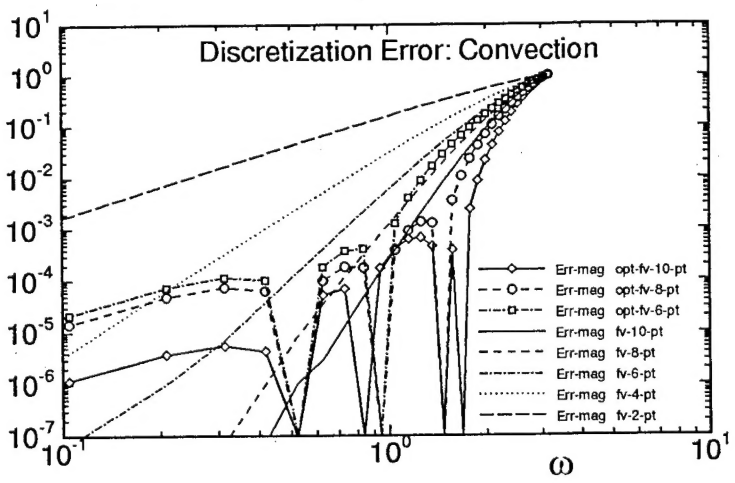


Figure 2.1(b) Error magnitude versus wave number for several finite-volume Talyor series and optimized approximations of a first derivative (logarithmic coordinates).

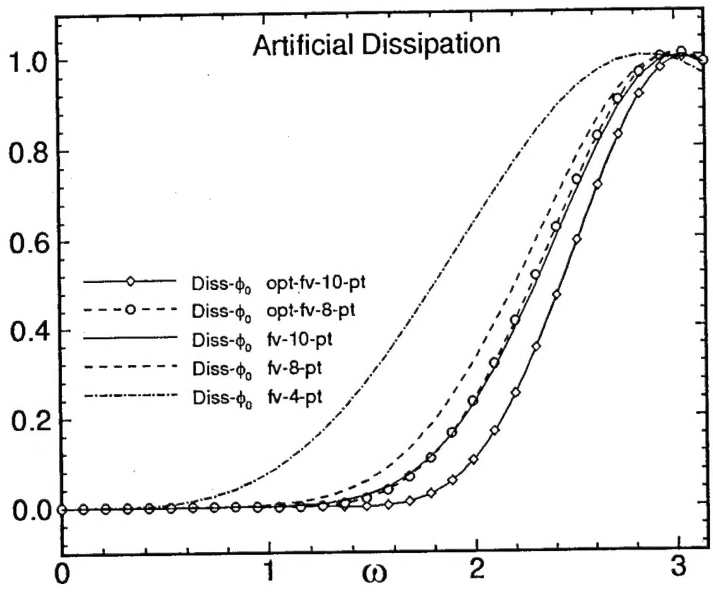


Figure 2.2(a) Finite-volume, artificial dissipation, optimized and Taylor series (linear coordinates).

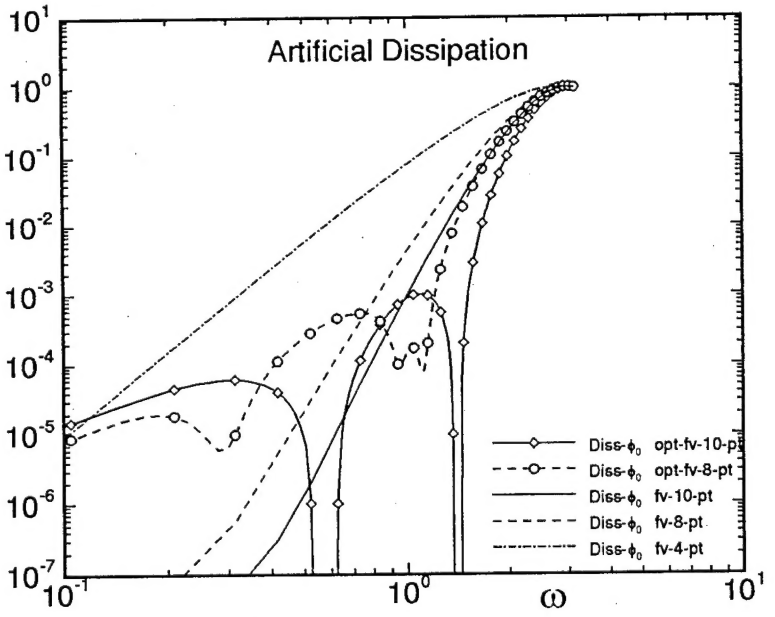


Figure 2.2(a) Finite-volume, artificial dissipation, optimized and Taylor series (logarithmic coordinates).

## 3. Compressibility Mechanisms

The broad goal of this work is to identify compressibility mechanisms which are important in high-speed turbulent flows. The effects of mean properties variation were postulated decades ago, are relatively well understood, and have been confirmed in several studies, including recent studies based on numerical simulations of turbulence (Coleman et al 1995, Huang et al 1995). A more specific objective of the present work is to understand the role of dynamical compressibility effects in high-speed turbulence. By the term dynamical compressibility, we mean the unsteady dilatation associated with the fluctuating vortical structures of turbulence. The clearest example of dynamical compressibility is in mixing layers and round jets, where the mixing rate decreases significantly and the structure of the dominant large scale vortices changes significantly at elevated Mach numbers.

Dilatation is the fundamental mathematical difference between the incompressible and compressible governing equation. This can be demonstrated by manipulating the Navier-Stokes equations (the conservation equations for mass, momenta, and energy) to be in a form that consist of the incompressible equation plus terms which scale on the dilatation. Thus, in the absence of dilatation, the equations revert to the incompressible equations. Because of this, the search for compressibility effects will start with observations of the dilatation interacting with other aspects of turbulence.

However, turbulence is a labyrinth of momentum and energy exchange mechanisms. The dynamical processes which dominate turbulence vary considerably among the different classes of turbulent flows. As observed in the present work, what would seem to be relatively low levels of dilatation apparently have the ability to significantly alter mixing layers, while boundary layer flows can experience higher dilatation (normalized by the local turbulence) without major changes in global characteristics (Childs & Reisenthel 1995). Thus, the occurrence or absence of high levels of dilatation does not ensure the presence or absence of significant compressibility effects. However, dilatation must be a key issue in compressible turbulence, and the interaction between vorticity and dilatation fluctuations should be especially important.

**Compressible Flow Equations** - The compressible Navier-Stokes equations can be written in the following form to illustrate the role of dilatation in distinguishing the compressible and incompressible equations.

$$\frac{1}{\rho}\frac{D\rho}{Dt}+\nabla\cdot u=0 \tag{3.1}$$

$$\rho\frac{Du_i}{Dt}-\frac{\partial p}{\partial x_i}-\frac{\partial}{\partial x_j}2\mu\{S_{ij}-\nabla\cdot u\,\delta_{ij}/3\}=0 \tag{3.2}$$

$$\rho\frac{De}{dt}+p\nabla\cdot u-2\mu\{S_{ij}S_{ij}-(\nabla\cdot u)^2/3\}+\frac{\partial}{\partial x_j}\left[k\frac{\partial T}{\partial x_j}\right]=0 \tag{3.3}$$

In which $S_{ij}$ is the conventional strain tensor and $\nabla\cdot u$ is the dilatation. Eliminating dilatation and variable properties ($\rho$ and $\mu$), the equations take on their incompressible form.

$$\frac{D\rho}{Dt}=\nabla\cdot u=0 \tag{3.4}$$

$$\frac{Du_i}{Dt}-\frac{1}{\rho}\frac{\partial p}{\partial x_i}-\frac{\partial}{\partial x_j}2\nu S_{ij}=0 \tag{3.5}$$

$$\rho C_v\frac{DT}{dt}-2\mu S_{ij}S_{ij}-\frac{\partial}{\partial x_j}\left[k\frac{\partial T}{\partial x_j}\right]=0 \tag{3.6}$$

Thus, dilatation is *the* mathematical difference between compressible and incompressible flows. Dilatation is easily identified in a simulation and provides a good starting point in a search for compressibility effects.

In addition to the dilatation, we are also interested in the fluctuating vorticity. The equation for the fluctuating vorticity magnitude in compressible flow can be written as follows.

$$\frac{D\langle\omega_i'\omega_i'\rangle}{Dt}=T_{\omega\omega}+P_{\omega\omega}+VS_{\omega\omega}+VD_{\omega\omega}+BCT_{\omega\omega}+\epsilon_{\omega\omega}$$

$$T_{\omega\omega}=-\frac{\partial}{\partial x_j}\langle u_j'\omega_i'\omega_i'\rangle+visc.$$

$$P_{\omega\omega}=-2\langle u_j'\omega_i'\rangle\frac{\partial\langle\omega_i'\rangle}{\partial x_j} \tag{3.7}$$

$$VS_{\omega\omega}=2\{\langle\omega_i'\omega_j'\rangle S_{ij}+\langle\omega_j'\rangle\langle\omega_i's_{ij}'\rangle+\langle\omega_i'\omega_j's_{ij}'\rangle\}$$

$$VD_{\omega\omega}=-\{\langle\omega_i\omega_i\rangle\langle\theta'\rangle+4\langle\omega_i'\rangle\langle\omega_i'\theta'\rangle+\langle\omega_i'\omega_i'\theta'\rangle\}/3$$

$$BCT_{\omega\omega}=2\{\langle\omega_i'(\nabla\rho'\times\nabla p')_i/\rho\rangle-\langle\omega_i'\rangle\langle(\nabla\rho'\times\nabla p')_i/\rho\rangle$$

in which T is transport, P is gradient production, VS is vortex stretching, VD is vorticity dilatation, BCT is baroclinic torque, and $\epsilon$ is dissipation. The viscous terms, transport and dissipation, are not written out explicitly because they are very messy in compressible flow. Their sum can be computed "by difference" in compressible flow, and the incompressible form is well known. The dominant terms in this equation in boundary layer turbulence are production via vortex stretching VS and dissipation $\epsilon$. There are two terms specifically associated with compressible (or variable density) flows, the vorticity-dilatation and baroclinic torque terms. The former of these is the greater in boundary layers, and it is significant in the global vorticity budget at elevated Mach numbers. The baroclinic torque appears to make a negligible contribution to the vorticity magnitude budget equation.

The reader is also referred to Lele (1994) for many other equations and further discussion of compressibility effects in turbulence.

**Summary of Known* Compressibility Mechanisms in Shear Layers (*although not without some controversy)** - Much is known about the effects of compressibility on turbulence. Some of the key facts are summarized here.

The clearest example of dynamical compressibility effects can be found in mixing layers. At convective Mach numbers as low as $M_c = 0.5$, the layer's growth rate is suppressed compared to incompressible flow. At higher $M_c$, vortices which are spanwise at low Mach numbers become oblique (or swept). To conserve streamwise vorticity, the dominant structure involves "criss-crossing" oblique vortices with opposite signs of streamwise vorticity. The dominance of oblique structures at elevated convective Mach numbers is predicted by linear theory, and observed in full nonlinear Euler and Navier-Stokes simulations and in experiments (Sandham & Reynolds 1989, Childs et al 1993, Goebel & Dutton 1991, Samimy et al 1992). Three simpler phenomena give rise to this vortical structure (Childs et al 1993): (1) The growth rate of a mixing layer composed of spanwise vorticies (e.g., in a 2D simulation) decreases to essentially zero at roughly $M_c \sim 1$, and remains small for all higher $M_c$. (2) In three-dimensional flows, this reduction in growth rate is determined by the effective convective Mach number, $M_{c,eff}$, which is the Mach number of the component of velocity normal to the structure. For swept structures, the effective velocity or $M_c$ is the conventional number scaled by the cosine of the sweep angle; for example, a structure swept nearly 90° would be in the streamwise direction. (3) The mixing layer growth rate is largely governed by the effective velocity difference normal to the structures. These three features interact to give swept structures at elevated $M_c$, and the resulting mixing layer has a sharply reduced growth rate compared to low-speed flows.

With the domination of oblique structures, the notion of the convective Mach number of mixing layer structures as viewed in the normal two-dimensional framework becomes imprecise. The dominant observable convecting features cannot be the oblique vortices themselves, which have no distinguishable x-position (in the conventional, x = streamwise direction notation) but must be some other feature <u>on</u> the vortex. For example, the vortex crossing points have well-defined x-positions, but these can also move due to lateral motion of the vortices.

Turbulent statistics from the high and low speed mixing layers reflect the vortical structure. Changes in the normal-stress anisotropy have been noted in experiment and simulations (Childs et al 1993, Goebel and Dutton 1990), but not seen in another experiment (Samimy et al 1992). (However, Samimy et al did observe the change in structure.) This anisotropy is attributed to the pressure-velocity statistics, which are in turn regulated by the vortex structure. The simplest explanation of these statistical processes is as follows: Energy enters turbulence as streamwise fluctuations $\overline{u'u'}$, and in low speed flow, the spanwise vortices rapidly couple these to vertical fluctuations $\overline{v'v'}$. However; the swept vortices a high-speed mixing layer more effectively couples $\overline{v'v'}$ and $\overline{w'w'}$ independent of $\overline{u'u'}$, which is the sole conduit of energy from the mean flow to turbulence. Thus, there is a reduced flow of energy into $\overline{v'v'}$, which is needed to generate shear stress and the energy in turbulence. This view of these statistical processes is quantified in Childs et al (1993).

The principal opposing theory of mixing layer compressibility effects has been one which postulates additional dissipation due to the dilatational velocity fluctuations, which simply weakens turbulence. One of several proponents of this theory was Zeman (1990), who developed a dilatation-dissipation theory at least in part based on turbulence simulation results which displayed "shocklets," or transient little shocks associated with the vortical fluctuations of turbulence. This theory still has supporters. However, there is now relatively widespread evidence from simulations of mixing and boundary layers that the dilatational dissipation is quite small, on the order of a fraction of a percent of the total dissipation. Shocks are generally not observed to be generated by simulated mixing layers even up to quite high speeds, like $M_c = 4$. (Childs et al 1993).

**Known Compressibility Mechanisms in Attached Boundary Layers** - Mean heating and variable properties effects on turbulent boundary layers are strong, and they are relatively well understood. The general framework for boundary layer compressibility effects (Van Driest) accounts for variable fluid properties, density and viscosity, but assumes incompressible kinematics within the boundary layer scaled for variable properties. Reviews of experimental data (e.g., Fernholz and Finley 1980) have demonstrated similarity in scaled mean properties for compressible and incompressible boundary layers. Recent simulations and analysis thereof by Coleman et al (1995) and Huang et al (1995) demonstrated that features such as the turbulent stress profiles up to $M=3$ under adiabatic-wall conditions collapse when properly scaled to account for variable properties.

Relatively subtle structural changes in the outer layer of boundary layers have been observed in experiments. The review by Spina, Smits, and Robinson (1994) cites several difference believed to be induced by elevated but moderate (e.g., $M_e<5$) Mach number. These include length scales, intermittency, and the structure of large outer-layer structures. Coleman et al (1995) also noted that the streaky structures of the laminar sublayer were straighter at $M_e = 3$ than at incompressible speeds.

A major anomaly in the study of compressible turbulence is the disparity between the strong dynamical compressibility effects in mixing layers and their virtual absence in typical boundary

layers up to $M_e=5$ or more. This problem is typically resolved to everyone's satisfaction by invoking Morkovin's hypothesis. The Mach number of typical velocity fluctuations in an attached boundary layer is typically much smaller than in a mixing layer and less than sonic. However, Morkovin's leaves some unresolved issues. For example, the linear evolution of the nascent mixing layer also satisfies the conditions of Morkovin's hypothesis, but it displays compressibility-induced changes.

Another reason that dynamical compressibility effects are weak in boundary layers can be attributed to the nature of the vortical structures in boundary layers. Outer layer structures move at a large fraction of the freestream velocity (e.g. 85 - 90%) and, given their extent and the velocity gradient, their convective Mach number would not be expected to trigger compressibility effects below a freestream Mach number on the order of $M\sim10$. The dominant inner-layer vortical structures tend to be streamwise vortices associated with loops or hooks into the log layer. The streamwise vortices are oriented so that any effective normal Mach number is small. Another factor is that the inner layer of an adiabatic-wall high-speed boundary layer is rather warm. The recovery factor is near unity for adiabatic-wall flows, and the sound speed at the wall scales on the freestream stagnation temperature. Under these conditions, the maximum Mach number based on the freestream velocity and the near-wall sound speed does not exceed 2.3.

In the next section, this background knowledge of compressible flow will be applied to results from boundary layer simulations. In many respects, the classical view of compressible boundary layers is observed: for example, the mean-isothermal M = 5 boundary layer more closely resembles an incompressible flow than does the adiabatic wall case at M = 5. However, phenomena are also identified which indicate that dynamical compressibility effects do occur in the mean-isothermal cases, and in adiabatic-wall flows at lower Mach numbers.

## 4. Boundary Layer Simulation Results

Simulations of boundary layers have been performed at freestream Mach numbers of $M_e$ = 0.5, 3, and 5, for Reynolds numbers in the range $400 \le Re_\theta \le 650$, and for adiabatic-wall (A-W) and mean-isothermal (M-IT) conditions. The flows are periodic in the streamwise and spanwise directions, which eliminates problems of inflow / outflow boundary conditions, in exchange for a temporally evolving boundary layer, rather than a spatially evolving one.

**Mean Boundary Layer Properties** - A few mean properties from the simulated boundary layers are presented here. There is little which is new in these results. The demonstration that the simulations yield the correct wall shear stress and reasonable mean velocity and temperature profiles serves principally to validate the simulations' accuracy. The small reduction in skin friction in the M-IT case, relative to the value given by the Van Driest theory, gives the hint that there may be differences in the turbulence at the effective Mach numbers generated by the cooling.

The skin friction coefficient is given in Fig. 4.1 for three A-W cases and the M-IT case. Simulation results are compared to the "Van Driest" theory (the Karman-Schönherr incompressible correlation modified by the Van Driest II compressible theory), which is reasonably accurate over a range of Mach and Reynolds numbers, and for adiabatic and cooled walls (Bradshaw 1977, Hopkins & Inouye 1971). Individual simulations generally yielded slightly different Reynolds numbers, and the theoretical curves are for the Reynolds number of the individual cases. The three A-W results are relatively close to Van Driest theory. The greatest error occurs at M = 0.5, which was the first boundary layer simulation performed during this effort, and which was probably not converged. The other two simulation results are slightly above the theory, but probably within its uncertainty band (Hopkins & Inouye 1971).

The M-IT result is compared directly to the Karman-Schönherr correlation, since there are no significant properties variations to generate effects via the Van Driest theory. It falls below the theoretical curve by roughly 15%, which is large enough to be considered significant. This discrepancy exceeds the uncertainty evident in the other simulation results, and it is greater than uncertainty in the Van Driest theory. Figure 4.2 gives the mean temperature profiles for the M = 5 A-W and M-IT cases.

The mean velocity profiles for the Me = 5, A-W and M-IT cases are given in Fig. 4.3, in modified log-layer coordinates. Instead of the typical $U^+(y^+)$ profile, $U^+$ is converted to $U^*(y^+)$ to account for mean viscosity and density variation by integrating the expression

$$dU^* = \left(\beta \frac{\mu}{\mu_w} + (1-\beta) \frac{\rho}{\rho_w}\right) dU^+ \qquad (4.1)$$

to obtain $U^*$, in which the weighting parameter $\beta$ is the ratio of viscous stress to the total stress:

$$\beta = \overline{\tau_{12}} / (\overline{\tau_{12}} + \overline{\rho u'' v''}) \qquad (4.2)$$

This expression is nothing more than a generalization of the expression used by Carvin et al (1988), which is made possible by simulations that resolve the near-wall viscous layer. The definition for $y^+ = u_\tau y/\nu_w$, with $u_\tau = \sqrt{\tau_w/\rho_w}$, is unchanged from the standard incompressible definition. The $U^*(y^+)$ profiles have the characteristics of a standard turbulence velocity profile, including a linear region, a log-layer, and a wake. The A-W results are actually fairly close to

$$U^+ = \frac{1}{\kappa} \log(y^+) + C_1 \qquad (4.3)$$

in which $\kappa = 0.41$ and $C_1 = 5$ are the usual coefficients, in the log-layer region. Data of Ferholz and Finley (1980) suggest that compressible profiles are close to this curve, but that a slightly larger value of $C_1$ might yield a better fit of data at the low values of $Re_\theta$ achieved in these simulations. However, these two simulations are not very different in Reynolds numbers, and thus, the difference in velocity profiles is not believed to be a Reynolds number effect. The reduced skin friction coefficient seen in Fig. 4.1 and the shifted velocity profile are consistent with a reduction in the inner-layer turbulent shear stress.

The second moment statistics, discussed next, reveal an even more complicated picture of the near-wall physics. Apparently conflicting dilatational processes are occurring: dilatation permits higher levels of wall-normal velocity fluctuations and thus shear stress in the very near-wall region, but some other dilatational mechanism suppresses shear stress further from the wall. The latter comment is based on observations of the sublayer streaky structure and the dilatation's affect on that structure, which are discussed in a later section.

**Second-Moment Statistics** - Second-moment statistics computed from the A-W cases of the present simulations were given in Childs and Reisenthel (1995) and are not repeated here. This discussion focuses on the compressibility effects seen in the M-IT cases, and how the second-moment statistics differ in the M-IT and A-W cases. In these results, all fluctuating velocities are normalized by the wall friction velocity, unless otherwise noted.

The RMS velocity fluctuations, given in Fig. 4.4, reveal a significant difference between the A-W and M-IT cases principally in $\overline{v'v'}^{1/2}$. At the wall, $\overline{v'v'}^{1/2} \sim y^+$ behavior is observed, rather than $\overline{v'v'}^{1/2} \sim y^{+2}$, which is normal for lower speed flows. This increase in $\overline{v'v'}^{1/2}$ is due principally to dilatation, because a strong correlation dilatation and $v'$ just above the wall was observed. The increase in $\overline{v'v'}^{1/2}$ near the wall is significant because it is the turbulent component of the source term for the turbulent shear stress. Relative to the A-W case, the near-wall behavior of $\overline{u'u'}^{1/2}$ is virtually unchanged, while the differences in $\overline{w'w'}^{1/2}$ are small but not negligible.

The turbulent shear stress from the M-IT simulation is also elevated near the wall, roughly $y^+ < 3$, and it differs significantly from the $|\overline{\rho u'' v''}| \sim y^{+3}$ behavior that is believed to apply to incompressible flows, as shown in Fig. 4.5. However, the elevated shear stress in the near-wall region is overshadowed by an even larger decrease between $y^+ \sim 3$ and the location of the maximum turbulent shear stress.

Another significant second-moment statistic is the (kinematic) shear stress correlation coefficient $R_{uv} = -\overline{u'v'}/(\overline{u'u'}\ \overline{v'v'})^{1/2}$. Figure 4.6 gives $R_{uv}$ for the A-W cases at M = 3 and 5, Spalart's (1988) simulation at M = 0, and the M = 5 M-IT case. The results from the three A-W cases are very similar, while the M-IT case shows a significant decrease in $R_{uv}$ in the region $y^+ < 15$, or roughly the thickness of the viscous sublayer. This is further evidence that a fundamental change in the kinematics of turbulence occurs near the wall in the mean isothermal case.

Turbulent Stress Budgets - The Reynolds stress transport equations offer yet another means of looking at the forces that govern turbulence. They are also the basis for several forms of turbulence models. The terms in the budget equations for the Favre-averaged forms of the turbulent kinetic energy, $\overline{\rho u_i'' u_i''}/2$ (using cartesian tensor notation), and the shear stress, $\overline{\rho u'' v''}$, are given in Figs 4.7 and 4.8. The components are relatively unambiguous, but to avoid any confusion, we note that the labels in the figures have the following meanings: "diffusion" denotes laminar transport, "transport" denotes turbulent transport via the triple products, and the "pressure-velocity" term is the native form, not split into the pressure-strain and pressure-diffusion parts.

Results are presented in Fig 4.7 for the turbulence energy in the M = 5, A-W and M-IT cases. While the gross features are similar in both cases, the following characteristics can be seen in the comparison of the M-IT and A-W cases. The peak in energy production is substantially broader in the M-IT case, and more similar to an incompressible flow (e.g., Spalart 1988). The effects of the elevated near-wall shear stress are evident in the increased near-wall energy production. As with the shear stress, however, turbulence energy production is lower in the M-IT case further from the wall. These results are consistent with the shear stress distributions for the two cases, given in Fig. 4.5. The turbulent transport of energy is roughly half as large in the M-IT case as it is in the A-W case, and it is more nearly like incompressible flow than the A-W flow. As with most changes in the buffer layer (i.e., roughly $5 < y^+ < 15$), variable properties are believed to cause this difference.

There is also one anomalous result near the wall that must be addressed. Near $y^+ \sim 2$ in the M-IT case, there is a discontinuous increase in the slope of the curve representing the diffusion of turbulence energy. When integrated to the wall, this slope discontinuity adds about 25% the

magnitude of the diffusion at the wall; the transport and dissipation terms also fail to sum to zero at the wall by about that same 25%. Nothing else in the results suggests that this behavior is physical, and we must conclude that it is an artifact of the numerical methods used. However, the source of the error has not been identified.

The shear stress budget terms are given in Fig. 4.8, and they display features which are consistent with the results presented in previous figures. As noted in the discussion of $\overline{v'v'}$, the shear stress production term in the near-wall region of the M-IT case is significantly larger than in the A-W case. However, the pressure-velocity term in the M-IT case is also larger by roughly the same amount. The role of turbulent transport via the velocity triple correlations is also substantially reduced in the M-IT case. A slope discontinuity in the viscous transport term for shear stress, similar to the one noted in the results for the turbulence energy, is also present; however, it is not easy to determine its significance, since the budget terms are nearly in balance at the wall.

Thus, in both the turbulence energy and shear stress, significant differences between the A-W and M-IT cases occur in the near-wall region. However, the more obvious and understandable difference, the near-wall increase in $\overline{v'v'}$ in the M-IT case is not the dominant one, since there is a decrease in the skin friction, not the increase that would be expected to accompany the increase in $\overline{v'v'}$. Knowing that the pressure-velocity term is principally responsible for suppressing the shear stress is sort of an intellectual "dead end" because so few details are known about the role of the pressure-velocity term in regulating the shear stress. However, the pressure-velocity term is believed to result from "structures" in turbulence. For example, the low pressure at vortex cores causes the interchange of energy in the $\overline{u'u'}$ and $\overline{v'v'}$ components, and this process also contributes to the pressure-velocity correlation.

In the final section of results, we examine interactions between the streaky structure of the viscous sublayer and fluctuating dilatation which may be the cause of the reduced shear stress in the M-IT cases.

**Dynamical Dilatation and Sublayer Streaks** - Statistical results indicate that important dilatational processes occur in the sublayer, and presumably therefore, involve interactions between dilatation and the streaks, which are the dominant structures in the sublayer. Dilatation is generally greatest at or very near to the wall, in all cases studied here. The regions of dilatation have a three-dimensional structure which is poorly understood, so far, but the structure can be reasonably complicated, at least in some instances. The present study has focused on the "footprint" of the dilataional regions, that is, the dilatation at the wall.

Composite figures which overlay dilatation, the streaky structure, and, in some figures, ejections and sweeps are given in Figs. 4.9 and 4.10. Some explanation of the details in those figures is required. The figures consist of a color contour plot with one or two overlying line contours in black and/or white. The color contours are one of two quantities, "sublayer height" or a "processed local shear stress" which is an indicator of bursts and sweeps. The "sublayer height" (denoted "SLH" in the figure) is the height (as $y/\delta_{99}$) at which $U/U_e = 0.4$. For the

Reynolds numbers considered here, this is a reasonable measure of the sublayer height. The processed shear stress ("ρuv" in the figure) is computed as

$$sign(v)\ \max(-\rho u'v', 0) \tag{4.4}$$

The max() operation retains only the shear stress which is of the same sign as the mean shear stress. The sign() operation assigns a positive sign to shear stress associated with positive $v'$ (bursts or ejections) and a negative sign to those with negative $v'$ (sweeps). Black contour lines denote fluctuating dilatation, with dashed contours being negative (compression). White contours denote sublayer height, when color contours are of the sweeps and bursts. This overlay of information is used to gain insight into the role of dilatation in the streak/burst process of the sublayer.

There are (at least) two processes with significance to the study of high speed boundary layer flows to be found in these results: the structure of dilatational regions offers some insight into the "compressibility effects" of flow over the sublayer streaks, and there is a difference in the streaky structure in the A-W and M-IT cases which is believed to be due to the effective Mach number ($U/c_w$) of the flows. Some observations of the nature of dilatation are listed here.

1. In general, the local maxima in dilatation magnitude occur on or immediately adjacent to the streaks. This is more apparent at high Mach numbers but also occurs at lower Mach numbers.
2. Dilatation tends to be associated with structures on the viscous streaks, for example at leading and trailing edges of streaks and sweeps or at kinks or curves along the streaks, but this is not universal.
3. Dilatation can occur in "packets" consisting of 5 to 10 extrema, on or adjacent to the streaks at the higher Mach numbers.
4. Streamwise vortical structures just above the sublayer (e.g., buffer layer vortices) can also be linked to dilatation at the wall. This linkage is not displayed in these figures.
5. Dilatation not linked to the streaky structure is often associated with sweeps.
6. Dilatation not obviously linked to any sublayer/buffer layer structure is also observed.
7. Changes in the average structure of individual dilatational regions occur with changes in the Mach number and the mean temperature profile (A-W or M-IT cases). At the highest effective Mach number ($M_e$ = 5, M-IT case), many dilatational regions tend to be oblique (swept) relative to the direction of the freestream, which is consistent with "supersonic relative motion" between the streaks and the local surrounding flow. Low speed flows do not generate oblique structures.
8. The size of an individual dilatational region depends on the structure it is associated with. The "roundish" dilational regions on the streaks have a mean diameter on the order of 10 in wall units, which is comparable to the height of the sublayer. The elongated dilatational regions associated with streamwise vortices just above the sublayer in the lower Mach number cases are roughly 10 wall units wide and 50 to 100 wall units long in the streamwise direction. The elongated oblique dilatational regions are roughly 10

wall units wide and 50 wall units long.

There is also a tendancy for the streaks to be straighter in flows at higher effective Mach number. In the $M_e = 3$ and 5 A-W cases, the streaks tend to meander (like a meandering river) and to branch. The occurence of meandering and branching streaks diminishes with higher effective Mach number in the M-IT cases. At the higher effective Mach numbers, the streaks which would have meandered are severed, so that the streaky structure consists of straighter sections of streaks separated by small gaps. This leads to more "leading edges"of streaks, and some of these appear blunted like a soft projectile after impact.

In a comparison of the sublayer streaks in A-W channel flows at M = 0 and 3, Coleman et al (1995) observed straighter streaks in higher Mach number flow. However, there was no further comment on the streaky structure or its relation with dilatation. Judging from the present results, the Mach number in those simulations was too low to generate a noticeable change in the pattern of dilatation. No other documentation of this change in the streaky structure at elevated Mach numbers was identified in the literature. However, the fact that Coleman's and the present simulations independently yielded very similar conclusions regarding the streaky structure suggests that this behavior is physical, and not an anomaly of the simulations.

Much of the dilatational structure is consistent with supersonic flow over the sublayer. Compressive dilatation (dashed contour lines for negative $\nabla \cdot U$) often occurs just upstream of a streak, while expansion (solid contour lines) occurs aft. Oblique dilatational regions and the dimunition of meandering of the streaky structure are also features expected in supersonic flow past a compliant object.

The global response of the boundary layer turbulence to dynamical compressibility effects on the sublayer are difficult to anticipate, since the dynamics of the sublayer structure are not that well understood (Robinson, 1991). Streaks and ejections are an essential part of turbulence energy generation in the buffer layer, and ejections tend to be associated with sinuous instability of the streaks. This association does not, however, imply a causative relationship between sinuous instabilities and ejections.

**Commonality of Dynamical Compressibility Effects?** - The dimunition of sinuous instabilities and the occurrence of oblique dilatational structures in boundary layers is somewhat similar to the compressibility-induced changes observed in high-speed mixing layers. Are there common mechanisms behind the behaviors of these two very different flows? We believe that the answer is a cautious "yes," for the following reasons.

A dominant effect in mixing layers is the change from spanwise vortices (circular in jets) at low speeds to oblique vortices at convective Mach numbers of roughly $M_c > 0.7$. This occurs because the growth rate of spanwise structures is sharply reduced at elevated Mach number, while oblique structures are amplified but at a lower rate than in the case of spanwise structures in incompressible flow. The theory describing this shift to three-dimensional modes is also based on the assumption that the most amplified modes will dominate a flow, which is reasonable for

an asymptotic mixing layer. It is also worth noting that the dilatation in mixing layers is relatively small, even at very high convective Mach numbers (e.g., $M_c = 4$, Childs & Reisenthel 1995).

There are numerous differences between the "local mean flow environment" of a mixing layer and a streak. Streaks are wakes consisting of two adjacent mixing layers, and the dominant incompressible mode is a sinuous instability. Furthermore, streaks are complex three-dimensional wakes. The dominant mode for an incompressible mixing layer consists of spanwise vortices. These dominant incompressible instabilities are present in streaks and mixing layers at low Mach numbers.

At elevated Mach numbers, the mixing layer structure is dominated by the three-dimensional mode which is the most amplified. In so doing, the normal stress anisotropy changes significantly in the mixing layer, because the oblique vortical structures strongly couple the two velocity components in a plane perpendicular to the axis of the vortex. In the mixing layer with nearly streamwise vortices, for example, there is a strong coupling between $v'$ and $w'$, both of which are weakly coupled to $u'$ (the streamwise component). The structures on streaks are not completely free to exploit three-dimensionality, since they are constrained by the wall and the broadly observed tendency of turbulence to generate flows with low fluctuating dilatation. Any oblique structures on the streaks would be required to have high levels of $u'$, $v'$, and $w'$. This is, however, exactly what is observed! Very near the wall in the M = 5 M-IT case, the RMS values of $v'$ are roughly 50% of the values of $w'$, which is an order of magnitude greater than observed in the M = 5 A-W case. Thus, there must be some strong mechanism pumping energy into $\overline{v'v'}$, which is likely to be the pressure-velocity correlation.

A second characteristic of mixing layer instabilities can also be seen in the sublayer. While the growth rate of high speed mixing layers experiences a steady decline with increasing Mach number, the shift to oblique structures occurs rather abruptly. This sudden shift to oblique structures is most clearly evident in the acoustic modes of high-speed jets at around M = 1.4 (Seiner 1984), and it is also explained by a simple theory based on the most amplified modes (Childs & Reisenthel 1995). A sudden transition which only occurs above a critical Mach number could explain why the shear stress correlation coefficient $R_{uv}$ displays no significant effect of Mach number up to the M=5, A-W case, but then changes significantly in the M=5, M-IT case.

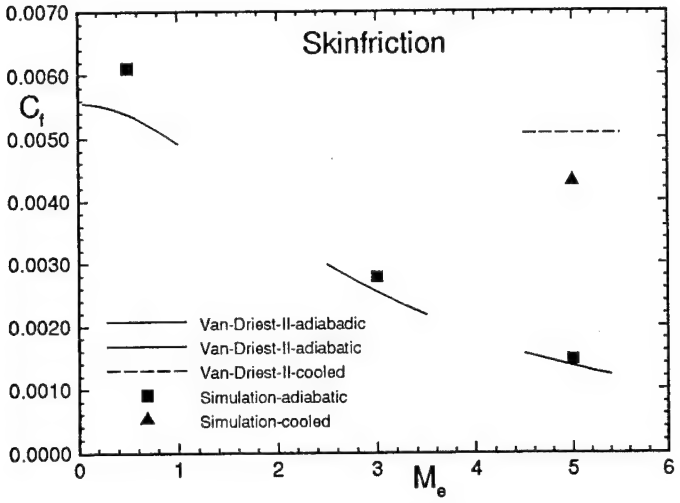


Figure 4.1 Skin friction from simulations and comparison to Karman-Schönherr correlation with Van Driest compressibility correction.

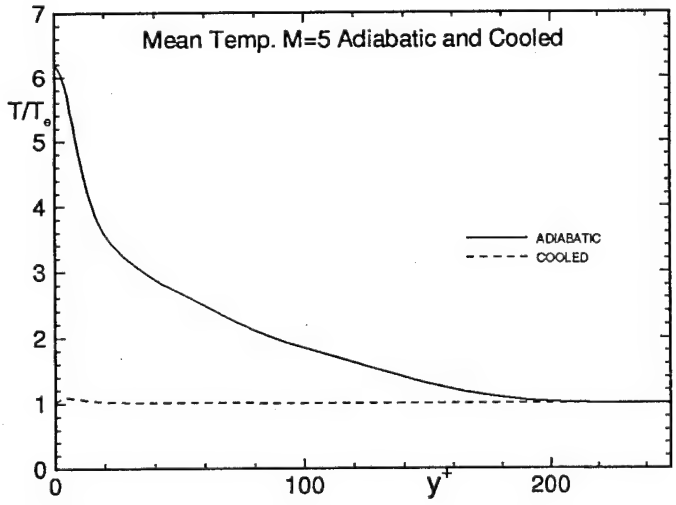


Figure 4.2 Mean temperature profiles in $M_e$ = 5 boundary layers, adiabatic and mean-isothermal cases.

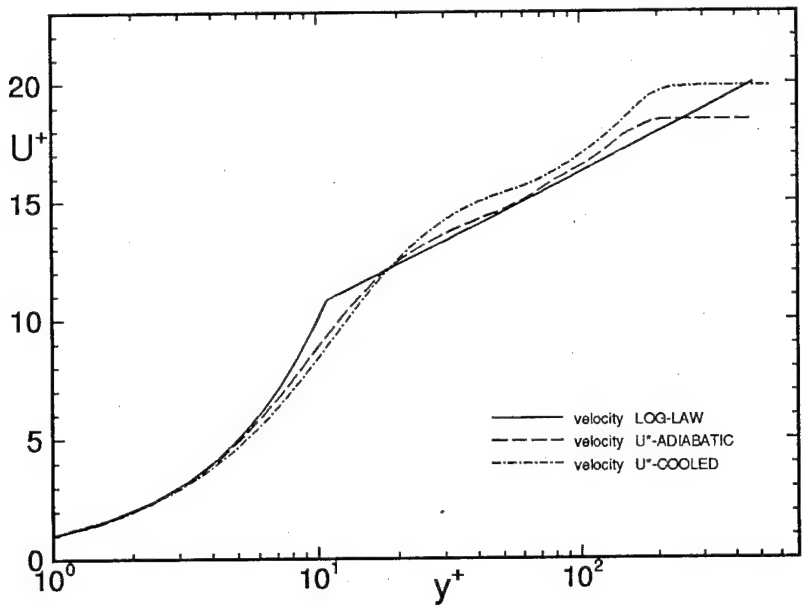


Figure 4.3 Mean velocity profiles for $M_e = 5$ boundary layer, adiabatic and mean-isothermal cases.

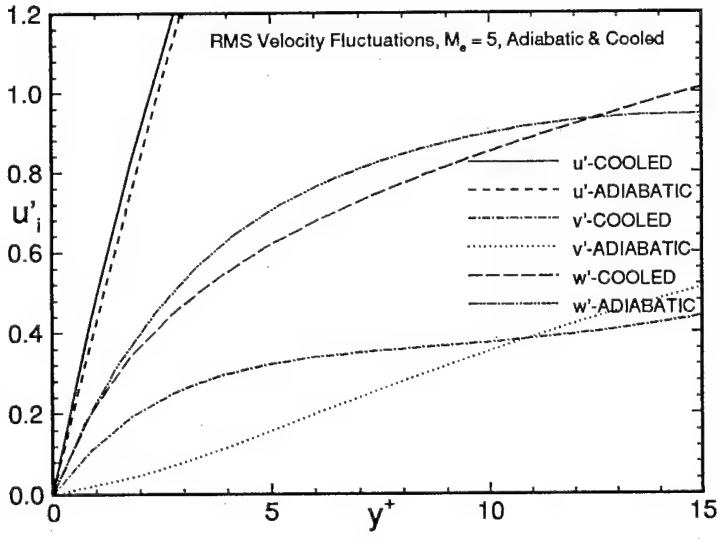


Figure 4.4 RMS turbulent velocity fluctuations for $M_e = 5$ boundary layer, adiabatic and mean-isothermal cases; inner layer.

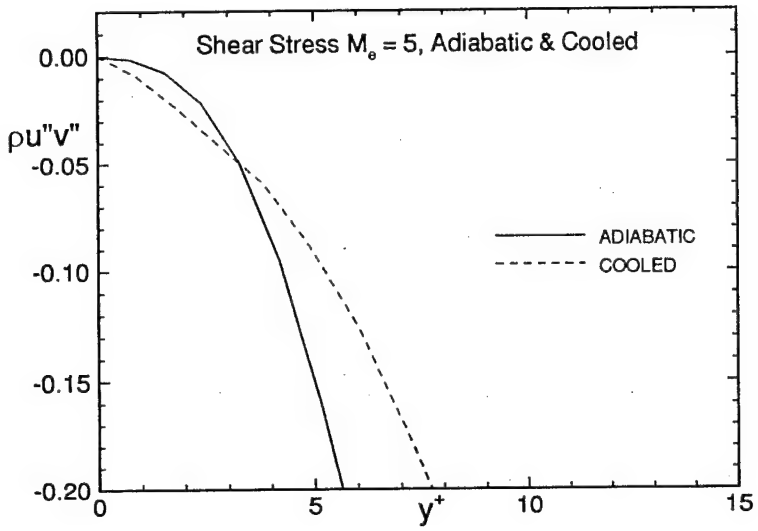


Figure 4.5(a) Shear stress for $M_e$ = 5 boundary layers, adiabatic and mean-isothermal cases, inner layer.

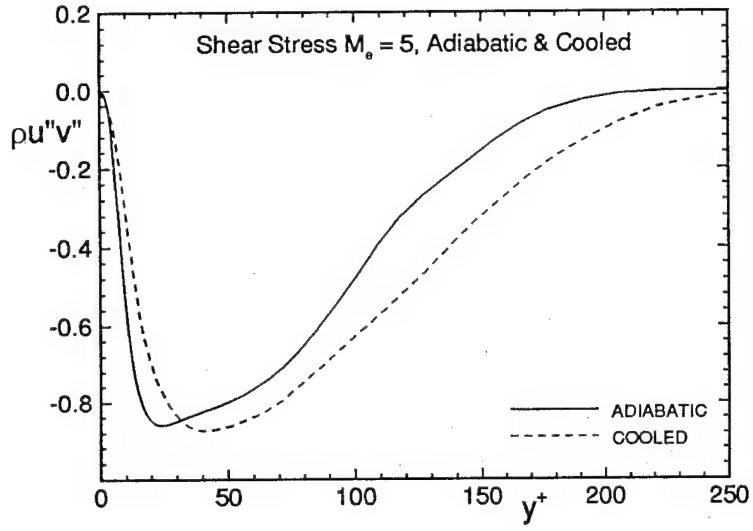


Figure 4.5(b) Shear stress for $M_e$ = 5 boundary layer, adiabatic and mean-isothermal cases, outer layer.

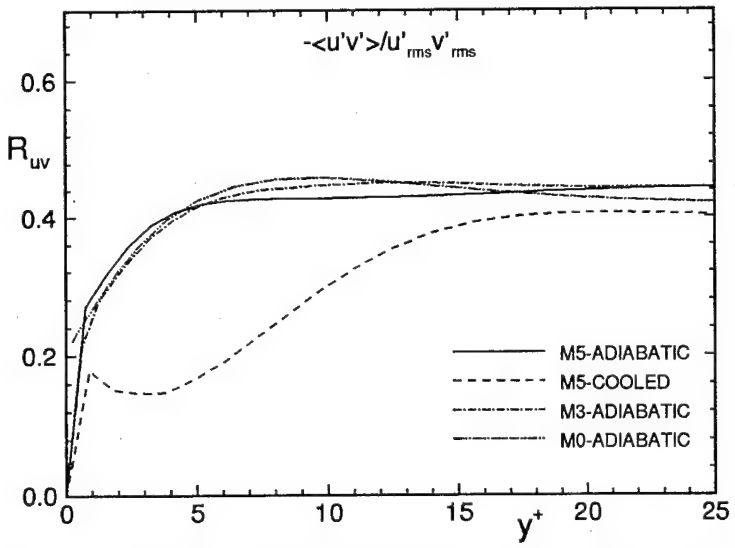


Figure 4.6 $R_{uv}$ correlation; adiabatic boundary layers at $M_e$ = 0, 3, 5, and mean-isothermal boundary layer at $M_e$ = 5. (M=0 results from Spalart, 1988)

1

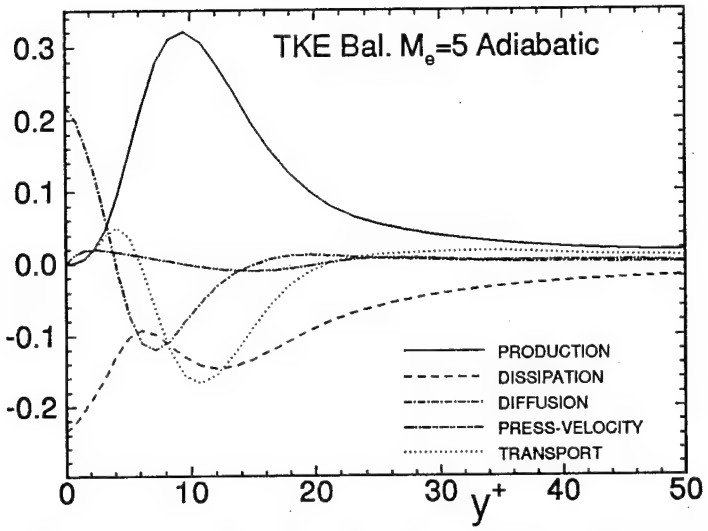


Figure 4.7(a) Terms in turbulent kinetic energy budget equation for M = 5, adiabatic boundary layer.

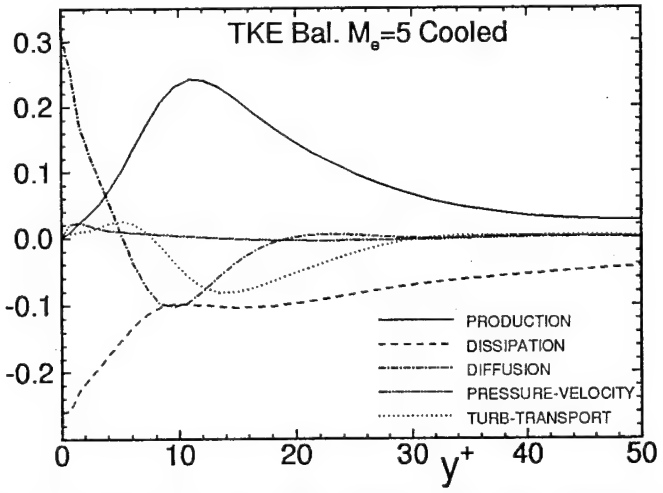


Figure 4.7(b) Terms in turbulenc kinetic energy balance equation for M = 5, mean isothermal boundary layer.

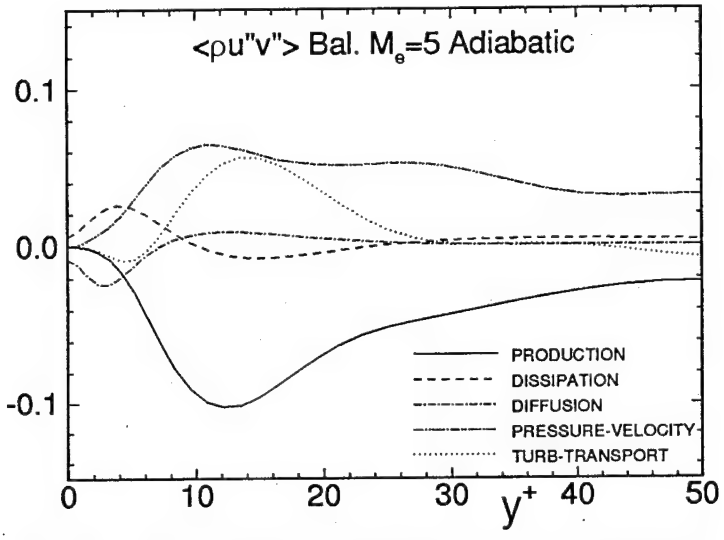


Figure 4.8(a) Terms in turbulent shear stress budget equation for $M_e = 5$ adiabatic boundary layer.

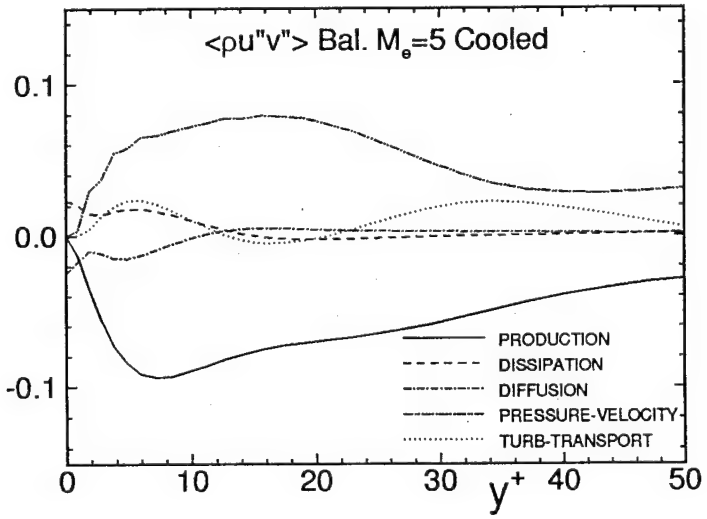


Figure 4.8(b) Terms in turbulent shear stress budget equation for $M_e = 5$ mean-isothermal boundary layer.

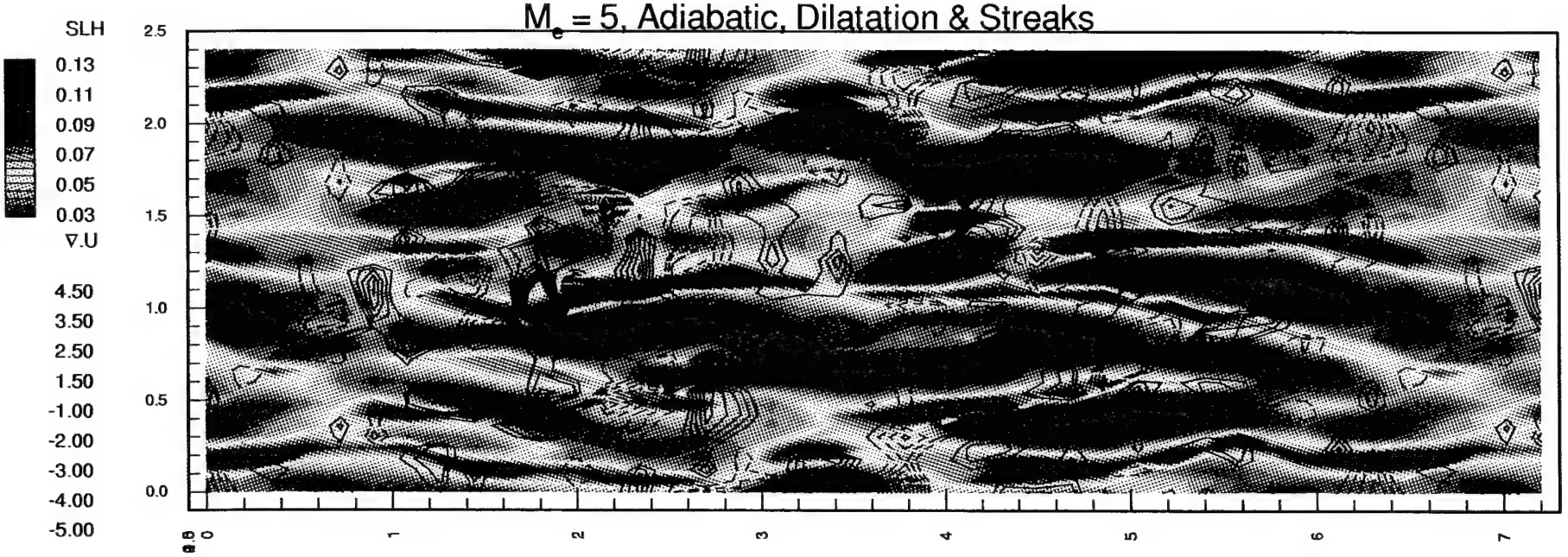


Figure 4.9 Composite overlay of sublayer streaks and dilatation, M=5 adiabatic-wall case.

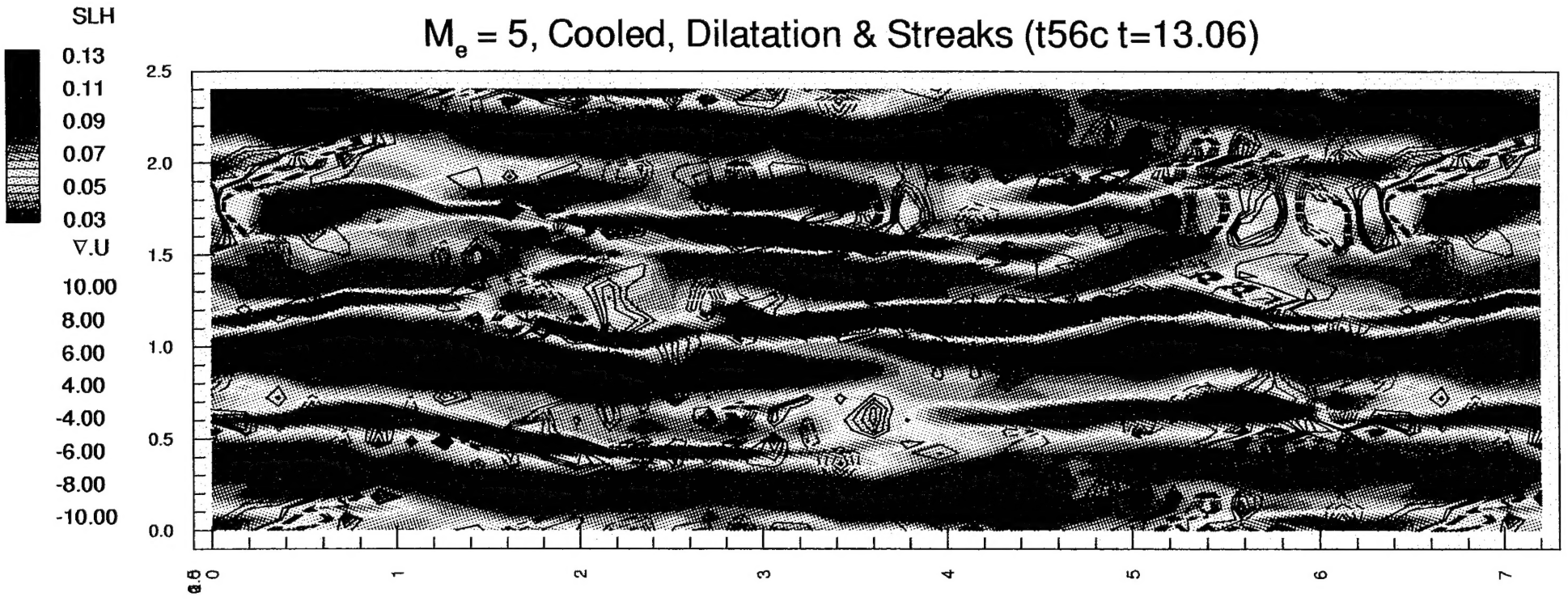


Figure 4.10 Composite overlay of sublayer streaks and dilatation, M=5 mean-isothermal case.

## 5. Conclusions

Numerical simulations have been used to study the effects compressibility on turbulence. Statistical and structural changes in turbulence are observed in both mixing layers and boundary layers. In mixing layers, the coherent large-scale vortices which dominate turbulent momentum transport change from being roughly spanwise at low convective Mach numbers to being oblique (swept towards the streamwise direction) at elevated convective Mach numbers, above roughly $M_c \sim 0.7$. The notion of the convective Mach number relating to the speed of structures becomes blurred when the structures are distributed in the streamwise direction and have no specific streamwise position to follow. However, the "convective Mach number" defined by the difference in velocities and the average sound speed is still used here. The structural changes are associated with large changes in the statistics for the normal-stress anisotropy, obviously in the shear stress, and in the pressure-velocity correlations.

In boundary layers, the computational artifice of deleting the mean dissipative heating has been used to generate mean-isothermal flows, to focus on dynamical compressibility effects. Under these conditions, a small but potentially significant decrease in the skin friction, relative to comparable incompressible conditions, is observed at $M_e = 3$ and 5. Numerous changes are observed in turbulent statistics and structures, relative to low speed flows, which are attributed to dynamical compressibility effects. Perhaps the most striking change is seen in the structure of viscous sublayer streaks. The streaks are sinuous at low Mach numbers, but they become straighter at elevated Mach numbers. Other structural changes are also observed. The dilatational field associated with the streaks has an oblique component, much like the oblique structures seen in mixing layers. Decreased sinuousness of streaks at elevated Mach numbers is also seen in simulations of Coleman et al (1995). Since sinuous instabilities are associated with bursting and thus help maintain turbulence levels in boundary layers, suppression of sinuous instabilities is consistent with the observed reduction in skin friction. There appear to be similarities between the compressibility mechanisms which affect mixing layers and those which alter the streaky structure.

## Bibliography


Blaisdell, G. A., Mansour, N. N., and Reynolds, W. C., (1994) "Compressibility Effects on the Passive Scalar Flux Within Homogeneous Turbulence," Phys. Fluids, Vol. 6, No. 10, 1994, pp. 3498-3500.

Bradshaw, P., (1977) "Compressible Turbulent Shear Layers," Ann. Review Fluid Mech., Vol. 9, pp. 35-54.

Carvin, C., Debeive, J. F., and Smits, A. J., (1988) "The Near-Wall Temperature Profile of Turbulent Boundary Layers," AIAA-88-0136.

Casper, J., Shu, C.-W., and Atkins, H., (1994) "Comparison of Two Formulations for High-Order Accurate Essentially Nonoscillatory Schemes," AIAA J., Vol. 32, No. 10, Oct. 1994, pp. 1970-1977.

Chakravarthy, S. R., Harten, A. and Osher, S., (1986) "Essentially Non-Oscillatory Shock-Capturing Schemes of Arbitrarily High Accuracy," AIAA-86-0339.

Childs, R. E., Rodman, L. C., and Nixon, D., (1992) "Methods for Computational Aeroacoustics," Nielsen Engineering & Research NEAR TR 452, August 1992.

Childs, R. E., (1993) "Prediction and Control of Turbulent Aero-Optical Distortion Using Large Eddy Simulation," AIAA-93-2670.

Childs, R. E., (1993) "Advanced Discretization Algorithm for CFD Methods," Nielsen Engineering & Research NEAR TR 469, July 1993.

Childs, R. E., Nixon, D., Keefe, L. R., and Rodman, L. C., (1993) "A Study of Compressible Turbulence," AIAA-93-0659.

Childs, R. E., (1994) Advanced Discretization Algorithm for CFD Methods, NASA Contract NAS2-14044, work in progress.

Childs., R. E. and Reisenthel, P. H., (1995) "Simulation Study of Compressible Turbulent Boundary Layers," AIAA-95-0582.

Chung, T. J. and Yoon, K. T. (1995) "Direct Numerical Simulation of Compressible Turbulent Flows Using Adaptive Spectral Element Method," AFOSR-TR-95-0051.

Clemens, N. T., Mungal, M. G., Hanson, R. K., and Paul, P. H., (1991) "Scalar Mixing in Supersonic Shear Layers," AIAA-91-1720.

Coleman, G. N., Kim, J., and Moser, R. D., (1994) "A Numerical Study of Turbulent Supersonic Isothermal-Wall Channel Flow," Submitted to J. Fluid Mech.

Fernholz, H. H. and Finley, P. J., (1980) "A Critical Commentary on Mean Flow Data for Two-Dimensional Compressible Turbulent Boundary Lyaers," AGARDograph AG253.

Ghosal, S., (1996) "An Analysis of Nuerical Errors in Large-Eddy Simulations of Turbulence, J. Comp. Phys., Vol. 125, pp. 187-206.

Goebel, S. G. and Dutton, J. C., (1991) "Experimental Study of Compressible Turbulent Mixing Layers," AIAA J., Vol. 29, No. 4, 1991, pp. 538-546.

Guo, Y. and Adams, N. A., (1994) "Numerical Investigation of Supersonic Turbulent Boundary Layers with High Wall Temperature," Proceedings of the Summer Program, 1994, Center for Turbulence Research.

Huang, P. G., Coleman, G. N., and Bradshaw, P., (1995) "Compressible Turbulent Channel Flows: DNS results and Modelling," J. Fluid Mech., Vol. 305, pp. 185-215.

Lele, S. K., (1992) "Compact Finite Difference Schemes with Spectral-Like Resolution," J.

Comp. Phys., No. 103, 1992, pp.16-42.

Lele, S., (1989) "Direct Numerical Simulation of Compressible Free Shear Flows," AIAA-89-0374.

Lele, S. K., (1994) "Compressibility Effects on Turbulence," Ann. Rev. Fluid Mech., Vol. 26, 1994, pp. 221-254.

Morkovin, M. V., (1962) "Effects of Compressibility on Turbulent Flows." In Mecanique de la Turbulence, ed. A. Favre, Paris: CNRS, 1962, pp. 367-380.

Moyal, J. E., (1952) "The Spectra of Turbulence in a Compressible Fluid; Eddy Turbulence and Random Noise," Cambridge Phil. Soc. Proc., Vol. 48, Part 2, 1952, pp. 329-344.

Oh, C. K. and Loth, E., (1995) "Unstructured Grid Simulations of Spatially Evolving Supersonic Shear Layers," AIAA J., Vol. 33, No. 7, 1995, p. 1229.

Reisenthel, P. H., Perkins, S. C., and Nixon, D., (1993) "A Study of Turbulence in Rarefied Gases," AIAA-93-3097.

Samimy, M., Reeder, M. F., and Elliot, G. S., (1992) "Compressibility Effects on the Large Scale Structure in Free Shear Flows," Phys. Fluids A, Vol. 4, No. 6, 1992, pp. 1251-1258.

Sandham, N. D. and Reynolds, W. C., (1989) "The Compressible Mixing layers: Linear Theory and Direct Simulation," AIAA-89-0371.

Sandham, N. D. and Reynolds, W. C., (1991) "Three-Dimensional Simulations of Large Scale Structure in Free Shear Flows," J. Fluid Mech. Vol. 224, pp. 133-158.

Seiner, J. M., (1984) "Advances in High-Speed Aeroacoustics," AIAA-84-2275.

Spalart, P. R., (1988) "Direct Simulation of a Turbulent Boundary Layer up to $Re_\theta = 1410$," J. Fluid Mech., Vol. 187, pp. 61-98.

Spina, E. F., Smits, A. J., and Robinson, S. K., (1994) "The Physics of Supersonics Turbulent Boundary Layers," Ann. Review Fluid Mech., Vol. 26, pp. 87-319.

Tam, C. K. W. and Webb, J. C., (1993) "Dispersion-Relation-Preserving Finite Difference Schemes for Computational Acoustics," J. Comp. Phys., No. 107, 1993, pp. 262-281.

Tam, C. K. W. and Dong, Z., (1993) "Wall Boundary Conditions for High-Order Finite-Difference Schemes in Computational Aeroacoustics," Theor. Comp. Fluid Dyn., Vol. 6, 1993, pp. 303-322.

Thompson, K. W., (1987) "Time Dependent Boundary Conditions for Hyperbolic Systems," J. Comp Phys., Vol. 68, No. 1, pp. 1-24.

Zeman, O., (1990) "Dilatation Dissipation: The Concept and Application in Modeling Compressible Mixing Layers," Pgys. Fluids A, Vol. 2, No. 2, pp. 178-188.

Zingg, D. W., Lomax, H., and Jurgens, H., (1993) "An Optimized Finite-Difference Scheme for Wave Propagation Problems," AIAA-93-0459.

Zingg, D. W. and Lomax, H., (1993) "Finite-Difference Schemes on Regular Triangular Grids," J. Comp. Phys., Vol. 108, No. 2, 1993, pp. 306-313.